Research Article

Liang Shi, Da Huo, Yanhua Lei*, Shaopeng Qu, Xueting Chang, and Yansheng Yin*

Effect of microstructure on tribocorrosion of FH36 low-temperature steels

https://doi.org/10.1515/htmp-2022-0034
received January 10, 2022; accepted April 08, 2022

Abstract: The tribocorrosion performance of low-temperature steels is vital for use in hostile environments. This study aims to investigate the tribocorrosion behavior of FH36 low-temperature steel with two distinct microstructures of tempered martensite (TM) and tempered sorbite (TS), respectively. Also, the coefficient of friction, surface morphologies, electrochemical properties, and corrosion features of the two steels were investigated. The results showed that the TM and TS steel exhibited outstanding impact toughness values of 239 and 306 J at −60°C, respectively. The friction coefficient and the electrochemical impedance in the TM steel were lower than those of the TS steel, while the scratch was deeper and narrower in the TM steel. Both the microstructure and the electrochemical corrosion affect the wear resistance of the low-temperature steels during the tribocorrosion process. The friction can accelerate the adsorption of Cl^- ions that enrich the pits near the scratches, and the pitting of the TM steel was severe.

Keywords: electrochemical impedance spectroscopy, polarization, microstructure, tribocorrosion, FH36 low-temperature steel

*** Corresponding author: Yanhua Lei,** College of Ocean Science and Engineering, Shanghai Maritime University, Shanghai 201306, China, e-mail: yhlei@shmtu.edu.cn
*** Corresponding author: Yansheng Yin,** Research Center for Corrosion and Erosion Process Control of Equipment and Material in Marine Harsh Environment, Guangzhou Maritime University, Guangzhou 510725, China, e-mail: ysyin@shmtu.edu.cn
Liang Shi: College of Ocean Science and Engineering, Shanghai Maritime University, Shanghai 201306, China; Institute of Science and Technology Information, Shanghai Maritime University, Shanghai 201306, China
Da Huo, Shaopeng Qu, Xueting Chang: College of Ocean Science and Engineering, Shanghai Maritime University, Shanghai 201306, China

1 Introduction

The Arctic is undergoing dramatic environmental change attributed to the warming climatic conditions [1]. There is increased interest in the development of Arctic mineral resources of oil and gas as the area of polar glaciers has shown a decreasing trend [2]. Low temperature and ice erosion are inevitable in the polar navigation of ships. Meanwhile, a large number of corrosive ions in seawater, especially chloride ions, will lead to the corrosion of metal materials. Tribocorrosion is a common phenomenon in steels that has gained increasing attention in ship and ocean engineering. Wear and corrosion co-occur during the ice-breaking process for the steels used as icebreaker sails, which will lead to the synergistic phenomenon of friction and corrosion of the ship hull [3]. Hence, tribocorrosion is one of the crucial problems for structural steels utilized in ship and ocean engineering, which plays a vital role in the service life and safety of structural steels.

Low-temperature steels possess excellent mechanical toughness and strength, making them suitable as structural steels in the polar regions [4,5]. The International Association of Classification Societies and the International Maritime Organization have defined the requirements of mechanical properties for the steels used in ship and ocean engineering [6]. Considering the service conditions, especially the ice environment, the steels can be divided into five grades [7]. Currently, grades F and FH are the highest grades of steels with high impact toughness properties at −60°C. In addition, the steels should also hold the merits of good mechanical properties, such as high yield strength, high tensile strength, and good ductility. However, properties related to applications, including friction, corrosion, and tribocorrosion, have not yet been mentioned. In the field of ship and ocean engineering, the tribocorrosion properties of structural steels should be considered in order to evaluate and predict their safety performance and service life, albeit their mechanical properties should fulfill the design requirements. Therefore, a comprehensive evaluation of the service

performance, especially the tribocorrosion of the ship and ocean engineering structural steels with advanced mechanical properties, is critical for their broad applications and long-term reliable usage.

The mechanical performance of the structural steels could be improved using two common ways. The first approach is to add alloy elements, such as titanium, nickel, niobium, and vanadium, which could refine the size of crystal grains and enhance the strength and toughness of the steels [8,9]. The second approach is to optimize the microstructures of the steels via heat treatments, which is economical for the microstructure regulation and enhancing the mechanical properties of the steels. It has been reported that the improvement of mechanical properties can be achieved by quenching and tempering by reduction of grain size, which was possible through thermomechanical cyclic quenching and tempering [10], quench-hardened [11], and electrolytic plasma hardening of steels [12]. Li et al. have studied the effect of temperature on microstructure and sliding wear behavior of low alloy wear-resistant martensitic steel, suggesting that the improvement of thermal strength was caused by delaying the decrease of dislocation density and carbide precipitation during the tempering of the martensite [13]. Studies proved that a hard martensite phase enhances the wear resistance of the steels [14,15]. In addition, researchers have also examined the effect of microstructure on the corrosion properties of metal materials. Hafeez et al. found that the corrosion rate dropped by cyclic quenching and tempering treatments of medium carbon low alloy steel due to the decrease in grain size [16]. Katiyar et al. investigated the comparative corrosion behavior of five microstructures of steels, namely, pearlite, bainite, spheroidized, martensite, and tempered martensite (TM) [17]. The results showed the variation of the corrosion rate in aerated 3.5% NaCl solution could be attributed to the shape, size, and distribution of the ferrite and cementite [17]. The morphological change of microstructure is an important factor affecting the corrosion sensitivity of steel [18]. Previous studies have focused on the steels' single wear or corrosion behavior. Nevertheless, these studies had some limitations. The synergistic interactions between wear and electrochemical corrosion were neglected in a real marine environment. To date, only a few studies have concentrated on the tribocorrosion behavior influenced by the microstructure of the steels. Liu et al. have reported the tribocorrosion behaviors of typical austenitic (ASTM 316), martensitic (ASTM S41500), and ferritic (ASTM S44660) stainless steels in a 3.5% NaCl solution under cathodic protection conditions and found that the wear rate and friction coefficient of austenitic steels were lower than those of ferritic and martensitic steels [19]. Some other studies have shown that, during the tribocorrosion process, the abrasion resistance of the steels is related to the microstructure [20]. However, this conclusion needs to be substantiated because the studied materials contain different chemical compositions, modifying the tribocorrosion behavior [21]. Besides, the effect of microstructure on tribocorrosion properties of low-temperature steels under heat treatments has not yet been investigated.

In the present study, we focused on the effect of microstructure on the tribocorrosion behavior of low-temperature steels. The 250°C TM and 650°C tempered sorbite (TS) microstructures of the FH36 low-temperature steel (after quenching/hardening) were first fabricated, which demonstrated excellent impact toughness. Friction, corrosion, and tribocorrosion tests were compared between low-temperature steels with microstructures of TM and TS, and the corrosive medium of 3.5 wt% NaCl solution was used. Also, the friction coefficient, morphology, electrochemical property, and corrosion scale of these two steels were investigated. Finally, the mechanism of the tribocorrosion process for low-temperature steels of two distinct microstructures was investigated.

2 Materials and methods

2.1 Materials and heat treatment

The FH36 low-temperature steel was provided by BAOWU Steel Co., Ltd. (China). The primary chemical components of the FH36 steel are listed in Table 1. To obtain two different microstructures, two heat treatment schedules were used. The steels were austenitized at 1,000°C for 1 h, followed by water-mediated cooling to room temperature. After tempering at 250 and 650°C for 1 h and the

Table 1: Chemical composition of the FH36 steel in wt%

C	Mn	Si	Cu	Cr	Ni	Mo	Al	P	S	Ti, Nb, V	Fe
0.055	1.25	0.18	0.22	0.12	0.72	0.01	0.039	0.008	0.001	0.036	Balance

subsequent cooling process, TM and TS steels were obtained, respectively. The whole heat treatment processes were performed in an argon atmosphere.

2.2 Mechanical properties

The tensile tests were investigated at room temperature using a WAW-600D Electronic Tensile Testing Machine (Jin'an Hansen Precision Instrument Co., Ltd., China), with a cross-head speed of 3 mm·min^{-1} according to ISO 6892-1:2009. The tensile tests of round specimens with a diameter of 8 mm and a length of 50 mm were investigated at room temperature, under a constant tensile load of 200 kN. The standard specimen (10 mm × 10 mm × 55 mm) with a v-notch parallel to the rolling direction was obtained, holding at −60°C temperature for 15 min in liquid nitrogen. The sample was taken out immediately, and then, the Charpy v-notch impact tests were carried out using a JBN-300C pendulum impact test machine (Ji'nan Shijin Group Co. Ltd., China). The average values of tensile, yield strength, and impact energy were averaged from at least three measurements. The surface hardness tests were conducted at 300 N on a digital display Brovi hardness tester (HBRVS-187.5; Dongguan Zhongte Co. Ltd., China).

2.3 Friction test

The samples of two steels after heat treatment were cut into specimens with a dimension of 10 mm × 10 mm × 3 mm. Then, the specimens were ground sequentially with carborundum papers from 200 to 800 grit and ultrasonically cleaned in ethanol and deionized water to remove dirty and oxide layers on the surfaces. The reciprocating friction and wear tests were carried out using a UMT TriboLab (Bruker, Germany). The counterpart was a Si_3N_4 ceramic ball of 5 mm diameter. A 30 N load was applied on the surface of the test specimens for 2 h. The sliding distance and speed were 5 mm and 10 mm·s^{-1}, respectively. The contact stress was calculated to be 525 MPa using Hertz contact theory [22]. The coefficient of friction (COF) was measured and recorded during the test. Three tests were repeatedly performed for each specimen to obtain the mean value.

2.4 Tribocorrosion test

The tribocorrosion test was carried out using an IviumStat potentiostat combined with a Bruker UMT TriboLab to study the wear and corrosion performance of samples in a 3.5 wt% NaCl solution at ambient temperature. The scheme of tribocorrosion is shown in Figure 1. The tribocorrosion device was integrated with a three-electrode cell configuration to monitor electrochemical properties. The parameters of the linear reciprocating friction process were the same as those mentioned in Section 2.3. The open-circuit potential (OCP) was monitored before sliding. Loading and rubbing were applied 50 min after OCP for stabilization, and then the wear test was performed under OCP in the 3.5 wt% NaCl solution for 2 h. During 2 h testing, the time history of COF was recorded. All tribocorrosion tests were performed three repeated times and exhibited good reproducibility.

2.5 Electrochemical test

The electrochemical tests were performed using an IviumStat potentiostat in a 3.5 wt% NaCl solution during corrosion and tribocorrosion processes at ambient temperature. The duration of the test was 2 h. A traditional three-electrode electrochemical testing configuration was applied, where the specimen was used as the working electrode with 1 cm^2 of the surface exposed to the electrolyte, Ag/AgCl as the reference electrode, and a Pt sheet as the counter-electrode. After stabilizing the specimens at OCP tracing, electrochemical impedance spectroscopy (EIS) measurements were performed at OCP with a sinusoidal potential wave of 10 mV at 10^{-2}–10^5 Hz. Then, the potentiodynamic polarization curves were acquired over a scan rate of 0.3 mV·s^{-1}, and the potential range was from −0.25 V_{OCP} to +0.5 V_{OCP}. The corrosion current density (I_{corr}) and corrosion potential (E_{corr}) were calculated using ZsimpWin software.

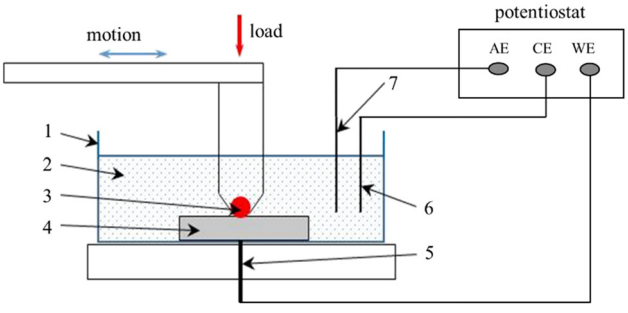

Figure 1: Scheme of the tribocorrosion electrochemical cell: 1, electrochemical cell; 2, solution; 3, Si_3N_4 ceramic ball; 4, specimen; 5, wire linking the specimen and the potentiostat; 6, silver/silver chloride (Ag/AgCl) as the reference electrode; 7, Pt wire as the counter-electrode.

2.6 Morphological analysis

The polished surface of the two steels was etched with a 3% Nital solution for approximately 10 s to reveal the microstructures. The phase identification of the two specimens was carried out by using a PANalytical X'Pert PRO X-ray diffraction (XRD), with Cu-Kα radiation (40 kV, 10 mA) and a scanning range from 10° to 80°. The surface morphologies were characterized by using a scanning electron microscope (SEM, JEOL, JSM-7500F, Japan) equipped with an energy-dispersive spectrometer (EDS). The corrosion products were removed according to the National Association of Corrosion Engineers method (1999). After friction, corrosion, and tribocorrosion tests, the morphologies of the steel specimens were detected by a Contour GT (Bruker, Germany) white light interferometer.

3 Results and discussion

3.1 Microstructure

Figure 2 shows the microstructures of the steels, and the rolling directions are marked by arrows. The specimen consisted of the microstructure of TM when the steels were tempered at 250°C, containing lath martensite, while the microstructure of TS consisted of quasi-polygonal ferrite and precipitate, when the steels were tempered at 650°C. The morphology of the microstructure of TS was similar to the previous study [23]. The laths in martensite continue to merge with increasing tempering temperature; ultimately, the quasi-polygonal ferrite formed by the decomposition of TM. Uniform microstructure provides a favorable guarantee for good strength and toughness. The precipitates were essential in the form of carbide, the fine carbide particles uniformly distributed in the ferrite matrix (as shown in Figure 2(d)), which could prevent dislocations from slipping and stabilized dislocation structures, thus delaying the fracture susceptibility of metallic materials [24].

Table 2 lists the mechanical properties of the two types of steels. The hardness values of TM and TS steels were 426.6 HV_{30} and 354.8 HV_{30}, respectively. The yield and tensile strengths of TM steels were 590 and 711 MPa, respectively, which were 26.1 and 24.7% higher than the corresponding values of TS steels (468 and 570 MPa), respectively. The higher heat treatment temperature (650°C) may cause the coarse growth of grains. The martensite will soften after high-temperature tempering. The lath martensite will change into polygonal ferrite, and carbide will precipitate at the same time. Meanwhile, the formation of carbides will also consume alloy elements, resulting in reducing the solid

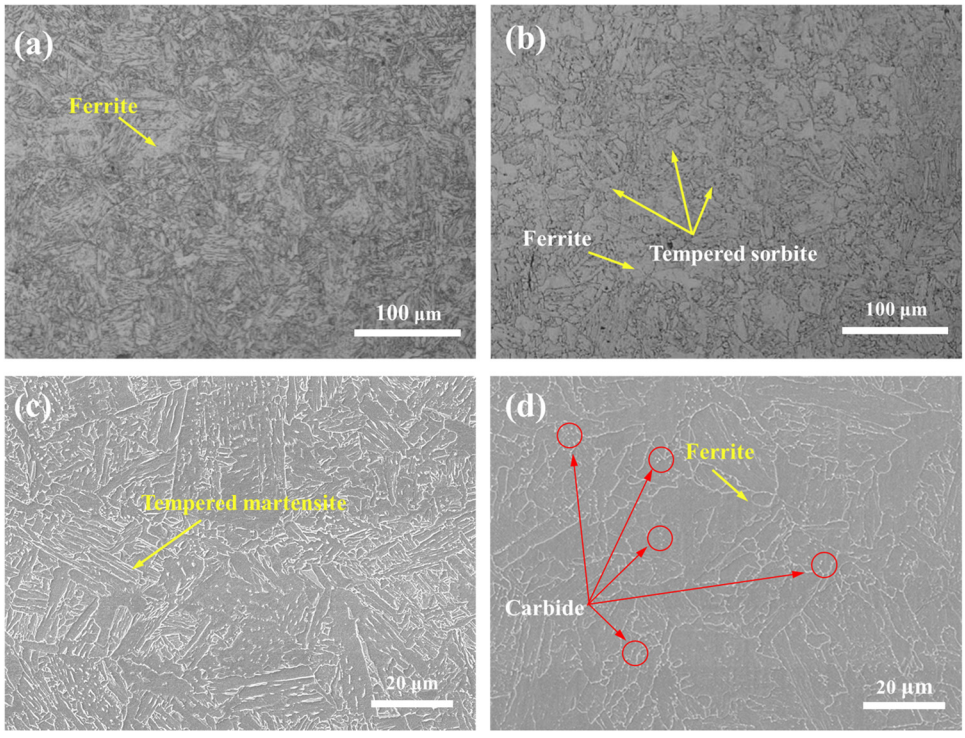

Figure 2: Microstructure of different samples: Optical microscopy of (a) TM and (b) TS steels; SEM images of (c) TM and (d) TS steels.

Table 2: Mechanical properties of TM and TS steels

Steel	Hardness	σ_s (MPa)	σ_b (MPa)	δ (%)	KV_2 (J) (at −60°C)	
	HV_{30}				Average	Minimum
TM	426.6	590	711	27.0	239	213
TS	354.8	468	570	30.2	306	288

solution strengthening effect near the ferrite boundary in the matrix structure [25]. The tensile strength, yield strength, and hardness of TS steels will decrease. The outstanding low-temperature toughness of both steels was achieved at 239 and 306 J at −60°C, respectively. Hence, it has been improved to meet the technical requirements in a low-temperature environment according to previous studies [26]. In fact, according to the service conditions of polar ships, the minimum impact toughness at −60°C should reach more than 34 J [27].

3.2 COF

The variation of the COF values of the specimens of TM and TS steels during the friction and tribocorrosion tests is presented in Figure 3. During the whole sliding tests, the two steels exhibited relatively stable friction properties with a constant friction coefficient. Notably, the COF of each steel during the tribocorrosion process was found to be less than that recorded in the friction process. In addition, tribocorrosion is known to be the result of the synergy of wear and corrosion. Thus, the presence of corrosion suggests the formation of some oxide lubrication of the tribointerface [28], which decreases the friction coefficient in 3.5 wt% NaCl solution.

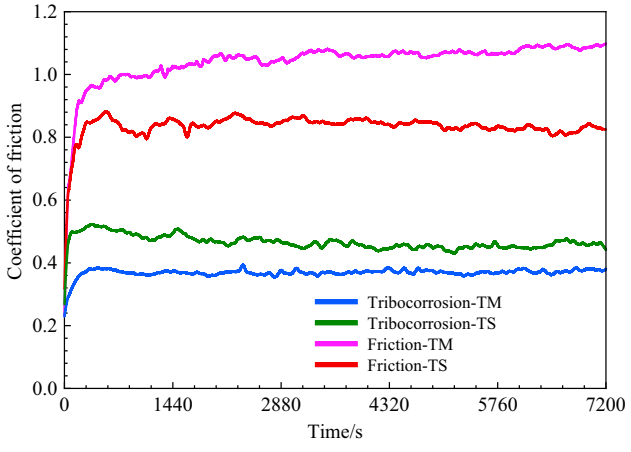

Figure 3: COF of TM and TS steels as a function of time during the friction and tribocorrosion processes.

Furthermore, the COF of the TM steel was higher than that of the TS steel during the friction process. Conversely, the COF of the TM steel was lower than that of the TS steel during the tribocorrosion process. This result confirms that the microstructure can affect the friction property of FH36 steel. As shown in Table 2, the strength of the TM steel is higher than that of the TS steel. Hence, the plastic deformation resistance of the TM steel was lower than that of the TS steel on the tested surface due to the value of yield strength and tensile strength, as shown in Table 2. However, the COF of the TM steel is lower than that of the TS steel during the friction test. Generally, the hardness affects the wear resistance. The higher the hardness, the smaller the wear rate, but the friction coefficient is not necessarily smaller. The COF often exhibits nonlinear dependency on the variables of hardness, the COF embodies all of the complexity that characterizes the contact, such as the shape of the abrasive and material response [29]. Trevisiol et al. underlined that the COF of the Archard law depends on the abrasive particle size [30]. As normal load increases and the friction coefficient decreases, the friction coefficient becomes insensitive to hardness. Nonetheless, the effect of the microstructure on the friction coefficient is more important than the effect of hardness.

Besides, wear resistance was dependent not only on hardness but also on thermal stability [31]. The oxidation layer occurs on worn surfaces, owing to friction heat under atmospheric conditions. It was possible because of the difference in delamination of tribo-oxide and wear debris size at the formed metal–metal interface, resulting in the decline of the COF of the TS steel during the friction test, in keeping with previous work [32]. The tribocorrosion of the TM steel showed the lowest COF, which could be attributed to the fine grains and presence of acicular martensite in the heat treatment process that might improve the tribocorrosion resistance; the synergistic effect of wear and corrosion also influences the COF of TM steel and TS steel in seawater. Distinguishing the effects of these two steels in friction and tribocorrosion tests revealed that both microstructure and corrosion affect the friction properties of low-temperature steels.

3.3 White light interferometry analysis

Figure 4 exhibits the white light interferometry images of the TM and TS steel specimens after the friction, corrosion, and tribocorrosion tests for 2 h. Figure 5 shows the profile lines of the surface morphologies shown in Figure 4, and the X-distance was parallel to the rolling distance of the steels.

Figures 4a and b and 5a and b demonstrate that the adhesive wear is the dominative wear mechanism during the friction test. The wear scar of the TS steel is larger than that of the TM steel, which is closely related to the microstructure size of the steels. The grain size of the TS steel is larger than that of the TM steel. Furthermore, the yield strength of the TM steel is higher than that of the TS steel, and hence, the deformation of the TS steel is lower

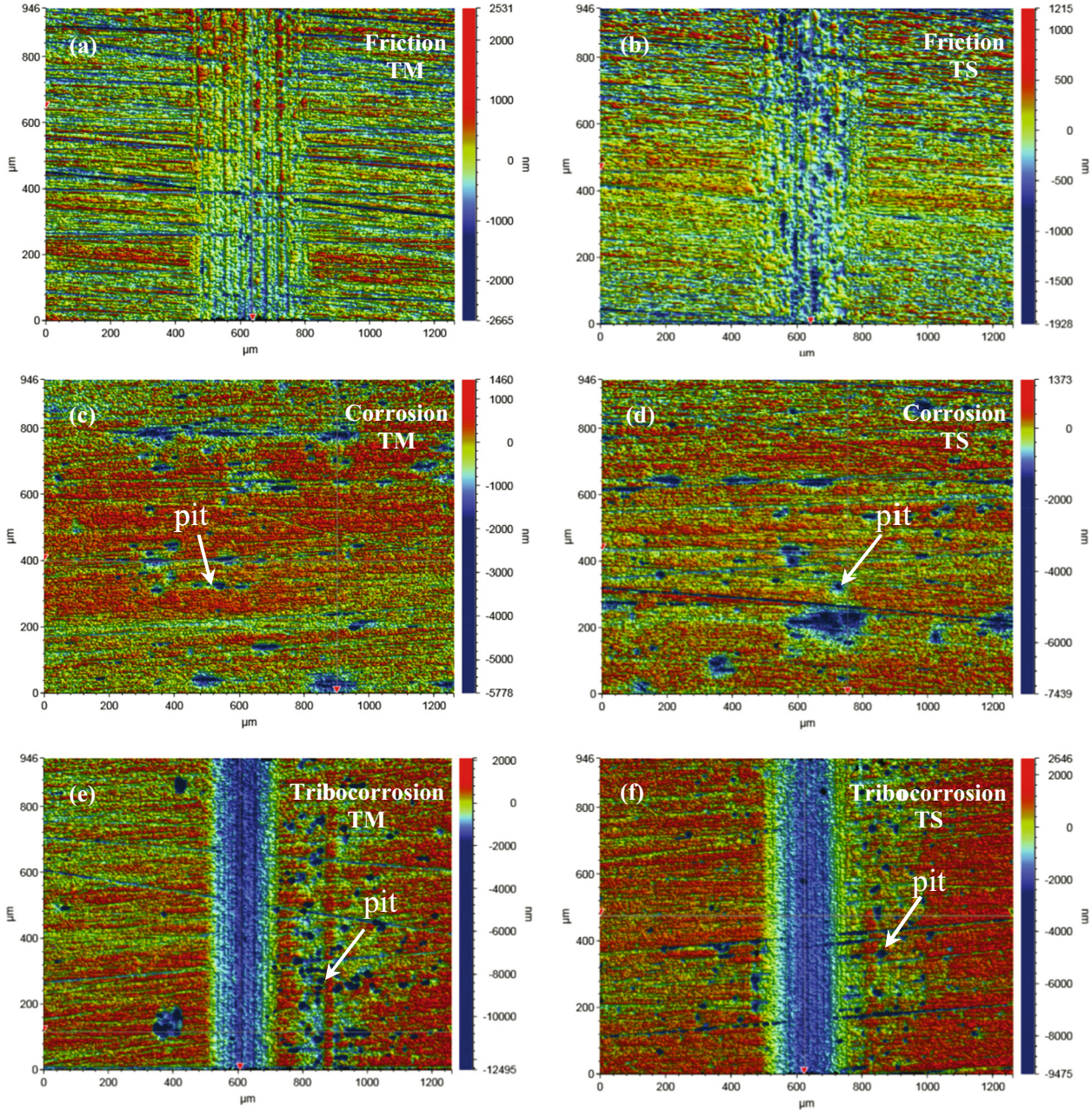

Figure 4: White light interferometry images of the surface morphologies of the different microstructure steel specimens without corrosion scales after the pure friction, corrosion, and tribocorrosion tests for 2 h. (a) TM steel after friction test; (b) TS steel after friction test; (c) TM steel after corrosion test; (d) TS steel after corrosion test; (e) TM steel after tribocorrosion test; and (f) TS steel after tribocorrosion test.

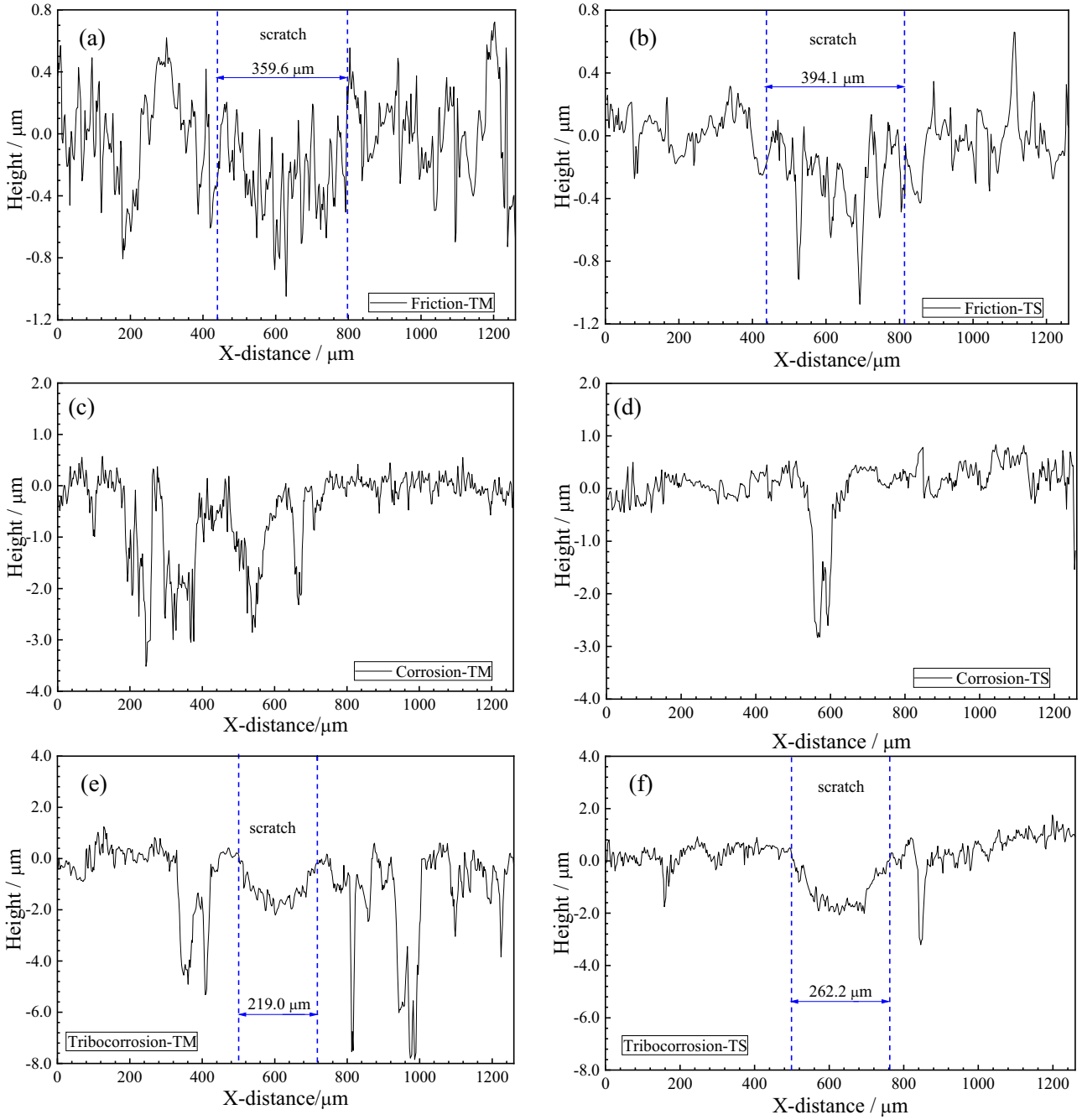

Figure 5: Profile lines of the surface morphologies of the different microstructure steel specimens after the friction, corrosion, and tribocorrosion tests for 2 h. Dash lines mark the boundary of the scratch. (a) TM steel after friction test; (b) TS steel after friction test; (c) TM steel after corrosion test; (d) TS steel after corrosion test; (e) TM steel after tribocorrosion test; and (f) TS steel after tribocorrosion test.

than that of the TM steel. In addition, the scratch of the TM steel (359.6 μm) is narrower than that of the TS steel (394.1 μm), which could be attributed to the higher yield strength of the TM steel. The maximum depth of the scratch for the TM steel is 1.05 ± 0.20 μm and that for the TS steel is 1.07 ± 0.17 μm.

For the corrosion test (Figures 4c and d and 5c and d), the morphology of the TM steel after the corrosion process was similar to that after the friction process. After immersion in the 3.5 wt% NaCl solution for 2 h, the corrosion pits, with a maximum depth of 3.0 μm, formed uniformly on the corroded surface.

However, the morphology of the TM steel differed markedly from that of the TS steel 2 h after the tribocorrosion test (Figures 4e and f and 5e and f). The pits were accumulated near the scratch, which was in accordance with the previous studies [33,34]. The diameters of the corrosion pits after the tribocorrosion test were obviously smaller than those after the corrosion test. However, the depth of the pits after the tribocorrosion test was deeper than that after the corrosion test. In addition, the maximum depth of the pit for the TM steel after tribocorrosion was about 7.9 μm, which was larger than that for the TS steel (3.2 μm). This indicated that pitting during the tribocorrosion process is more serious than that during the corrosion process, and pitting for the TM steel is more serious than that for the TS steel during the tribocorrosion process. Furthermore, the maximum depths of the scratch for TM and TS steels are 7.21 ± 0.13 μm and 3.37 ± 0.15 μm, respectively, 2 h after the post-tribocorrosion test. Moreover, the wear depths of both steels after the tribocorrosion test were about two-fold deeper than those after the corrosion test. The width of the scratch for the TM steel (219.0 μm) was narrower than that for TS steel (262.2 μm) after the tribocorrosion test, and both were narrower than those after the friction test.

Based on the above findings, it could be speculated that the wear loss during the tribocorrosion process is accelerated by corrosion compared to the wear loss during the friction test, and the wear loss for the TS steel is larger than that for the TM steel during the tribocorrosion test. During the processes of friction and tribocorrosion, the widths of scratch for the TS steel were wider than that for the TM steel. This phenomenon could be attributed to the higher strength of the TM steel than that of the TS steel, which renders the deformation of the TS steel easier and the width of the scratch wider than the TM steel. In addition, irrespective of the microstructure of the steel, the width of the scratch during tribocorrosion is narrower than that during friction. This could be due to the varied forces of friction. Figure 3 clarifies that the COF during the tribocorrosion process is lower than that during the friction process, and hence, the force of friction during tribocorrosion is low. Collectively, the corrosion products, together with the corrosive medium on the surface of the steels, show solid lubricious properties that reduce the force of friction during the tribocorrosion process compared to the friction process. Therefore, the deformation of the steels is serious, and the scratch is narrower during tribocorrosion than that during friction.

3.4 Electrochemical analysis

Table 3 shows the OCPs of TM and TS steels at 50 min during corrosion and tribocorrosion tests. The TM steel exhibit relatively lower OCP during the corrosion and tribocorrosion period than the TS steel. All the OCPs declined during the tribocorrosion test compared to the corrosion test, indicating that the friction can reduce the OCPs of the steels during the corrosion process. The mechanical wear thinned or removed the corrosion products formed on the steels when the friction began [35], thereby exposing the fresh surface to the corrosive media and decreasing the OCP.

Figure 6 shows the EIS and potentiodynamic polarization curves of TM and TS steels during corrosion and tribocorrosion tests. Figure 6a shows that the corrosion resistances of TM and TS steels are similar during the corrosion process, while the corrosion resistance decreases during the tribocorrosion process, especially for the TM steel. These results proved that the corrosion is accelerated by friction during the tribocorrosion process, and the corrosion of the TM steel is easier than that of TS steel during the tribocorrosion process. In addition, the inductance contraction occurs at a low frequency, which is mainly caused by Cl^- adsorption on the corrosion surface [36,37]. The EIS results show that Cl^- adsorption is more severe during the tribocorrosion process than that during the corrosion process, and Cl^- is a harmful ion for corrosion that could induce pitting [38,39]. Hence, pitting is more severe during the tribocorrosion process than that during corrosion, as shown in Figures 4 and 5. Interestingly, the combination of declined corrosion resistance and increased Cl^- adsorption for the TM steel during the tribocorrosion process could lead to severe pitting; these phenomena explain why pitting is deeper for the TM steel during the tribocorrosion test (Figure 5e).

Figure 6b shows that the corrosion process is controlled by the cathodic process, which is regulated by the diffusion of oxygen into the iron, and the anodic process is controlled by polarization. The TM and TS

Table 3: OCPs of TM and TS steels at 50 min during corrosion and tribocorrosion tests (vs Ag/AgCl)

Steel	Corrosion test (V)	Tribocorrosion test (V)
TM	−0.691	−0.710
TS	−0.663	−0.693

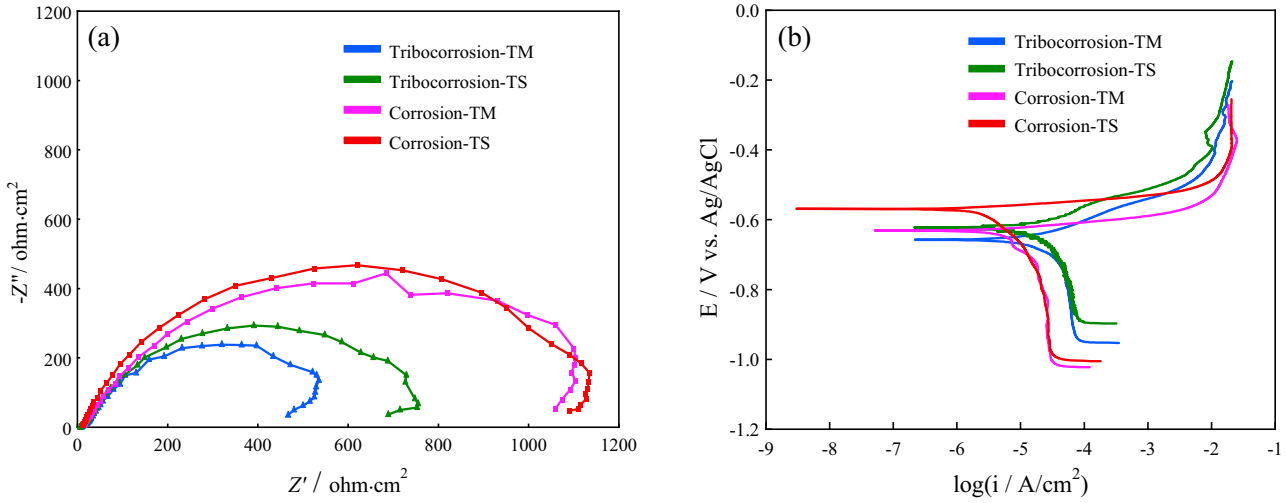

Figure 6: The electrochemical results of the different microstructure steel specimens during the corrosion and tribocorrosion tests. (a) EIS; (b) potentiodynamic polarization curve.

steels after corrosion and tribocorrosion characteristics were further analyzed by the equivalent circuits, as shown in Figure 7. Data were fitted with built-in software of Zsimpwin (Table 4).

In the equivalent circuits, R_s represents the solution resistance, Q_{dl} represents the double-layer capacitance on the surface of the electrolyte solution and the steel samples, Q_f and R_f represent the capacitance and resistance of the insoluble corrosion products formed during immersion, respectively, and R_{ct} represents the charge-transfer resistance. The impedance Q is calculated using equation (1), where ω represents the angular frequency and Y_0 and n represent positive integers. In the above equation (1), $n = 1$ represents the ideal capacitor, $n = -1$ represents inductance, and $n = 0.5$ represents the Warburg impedance:..

The capacitance can be calculated from the experimentally determined constant phase element (CPE) parameters using equation (2):

$$C = \omega^{n-1} \cdot Y_0 \cdot \sin(n\pi/2), \quad (0 < n < 1). \tag{2}$$

As shown by fitting parameter results, in the bacterial culture, the solution resistance (R_s) decreased significantly from static corrosion to tribocorrosion, indicating that tribocorrosion affected the solution conductivity. The R_f showed a similar tendency, indicating that the formation of corrosion products decreased. R_{ct} also shows a decreasing trend that can be attributed to the product film, which inhibits its electron transfer and penetration of the corrosive ions. The values of R_{ct} of TM and TS steels changed little in pure corrosion conditions, while the TS steel had higher charge-transfer resistance (767.2 Ω·cm^2) than the TM steel (554.3 Ω·cm^2) in tribocorrosion. This might be related to the carbides dispersed and precipitated in TS steels, evenly distributed in the matrix, which improved the corrosion resistance [40].

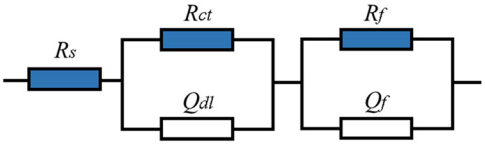

Figure 7: The equivalent circuit used for fitting the impedance data of the TM and TS steels.

The values of electrochemical corrosion of polarization curves, such as corrosion potential (E_{corr}), corrosion current density (I_{corr}), polarization resistance (R_p), cathodic Tafel slope (β_c), and anodic Tafel slope (β_a) are listed in Table 5. I_{corr} was calculated using the Stern–Geary equation, given as:

$$I_{corr} = \frac{\beta_a \beta_c}{2.303(\beta_a + \beta_c)} \times \frac{1}{R_p}. \tag{3}$$

The corrosion current densities are 0.073 and 0.069 mA·cm^{-2} for TM and TS steels, respectively, during the corrosion test, which increase twofold during the tribocorrosion test (0.193 and 0.136 mA·cm^{-2}, respectively). This indicates that friction increases the diffusion of oxygen (as a depolarizer during the corrosion reaction) in the 3.5 wt% NaCl solution, which could explain the accelerated corrosion during the tribocorrosion process. Furthermore, the corrosion potential of the two steels declined obviously during the tribocorrosion test compared to that during the

Table 4: Electrochemical fitting parameters of TM and TS steels after corrosion and tribocorrosion

Steel	R_s ($\Omega \cdot cm^2$)	Q_f		R_f ($\Omega \cdot cm^2$)	Q_{dl}		R_{ct} ($\Omega \cdot cm^2$)
		Y_f ($\Omega^{-1} \cdot cm^{-2} \cdot s^{nf}$)	n_f		Y_0 ($\Omega^{-1} \cdot cm^{-2} \cdot s^n$)	n	
Corrosion-TM	10.37	6.187×10^{-4}	0.601	41.79	9.04×10^{-5}	0.838	1115
Corrosion-TS	9.88	2.303×10^{-4}	0.522	46.94	5.129×10^{-5}	0.873	1108
Tribocorrosion-TM	8.385	3.136×10^{-4}	0.585	20.71	1.602×10^{-4}	0.850	554.3
Tribocorrosion-TS	6.152	1.243×10^{-4}	0.705	15.42	1.451×10^{-4}	0.818	767.2

corrosion test, which is mainly because of the friction on the corroded surface. The friction increases the dislocation density and promotes the deformation around the scratch on the corroded surface. The dislocations and deformations would increase the electrochemical activity of the steels [41,42], which decreases the corrosion potential of the steels. The mechanochemical effect also suggested that the stress applied to the steels could decrease the corrosion potential [43]. In addition, the corrosion potential of TM steel was lower than that of the TS steel during both corrosion and tribocorrosion tests. This phenomenon could be attributed to the decline in the dislocation density and residual stress of the TS steel by higher temperature tempering (650°C) compared to that of the TM steel (250°C), which increases the corrosion potential of the TM steel.

3.5 Corrosion scale analysis

Figure 8 shows the corrosion scales of TM and TS steels after corrosion and tribocorrosion tests for 2 h. Figure 8a and b shows the flocculent corrosion scales formed on the corroded surfaces of TM and TS steels, respectively, after the 2 h corrosion test. The EDS results showed that the corrosion products mainly contain Fe, O, C, and Cl elements, and the proportions of O elements of TM and TS steels were about 19.75 and 15.81 wt%, respectively. However, the proportions of Cl elements on the surface of the two steels did not differ markedly; the distribution of corrosion scales was uniform and dispersive, and the corrosion products of TM and TS steels were similar.

However, the distribution of corrosion scales on the corroded surfaces of TM and TS steels after tribocorrosion test was different from that after the corrosion test, while the distribution of the corrosion scale for the TM steel was similar to that for the TS steel after the tribocorrosion test. Both could be divided into three zones (Figure 8c and d): scratch, near scratch, and distant. Herein, we observed that the corrosion scales were mainly accumulated in the near-scratch zone. The EDS marked with a red cross in Figure 8c and d showed that the corrosion scale mainly contains Fe, O, C, and Cl elements but O and Cl elements after the 2 h tribocorrosion test (Table 6).

According to Table 6, the Cl element is enriched in the near-scratch zone after the tribocorrosion test, and the content of the Cl element after the tribocorrosion test is higher (about 2.12 wt%) than that after the corrosion test (about 0.25 wt%). Moreover, Cl^- induces pitting during the corrosion process, and hence, the pits concentrate near the scratch and are more severe during the tribocorrosion test than that during the corrosion test. In addition, the O element is enriched in the near-scratch zone but is reduced in the scratch zone after the 2 h tribocorrosion test. Thus, the volume of the O element indicates that the corrosion products are abundant in the near-scratch zone, while a few appear in the scratch zone after the tribocorrosion test.

XRD was employed to determine the composition and chemical states of the surface of samples. Figure 9 illustrates the surfaces of the TM and TS steels before and

Table 5: Parameters of potentiodynamic polarization curves in Figure 7b after 2 h of immersion

Specimens	E_{corr} (V vs SCE)	I_{corr} ($mA \cdot cm^{-1}$)	R_p ($k\Omega \cdot cm^{-1}$)	β_c ($mV \cdot dec^{-1}$)	β_a ($mV \cdot dec^{-1}$)
Tribocorrosion-TM	−0.638	0.193	63.647	−0.123	0.023
Tribocorrosion-TS	−0.621	0.136	69.731	−0.039	0.014
Corrosion-TM	−0.631	0.073	79.858	−0.113	0.012
Corrosion-TS	−0.569	0.069	75.125	−0.140	0.011

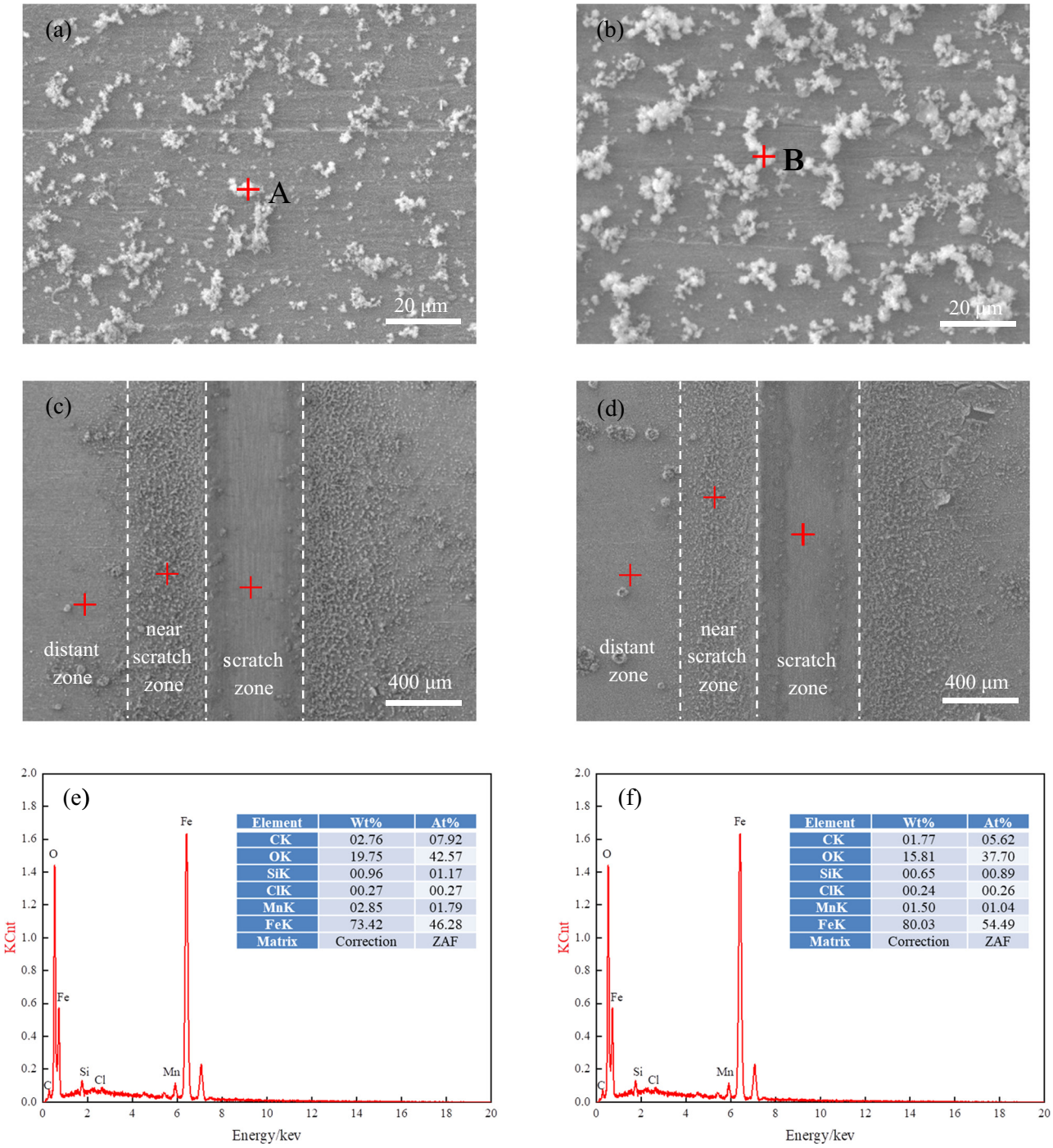

Figure 8: Corrosion scales of the different microstructure steel specimens after corrosion and tribocorrosion tests for 2 h. (a) TM steel after corrosion test; (b) TS steel after corrosion test; (c) TM steel after tribocorrosion test; (d) TS steel after tribocorrosion test; (e) EDS result of point A in Figure 7a; and (f) EDS result of point B in Figure 7b.

after immersion in the 3.5 wt% NaCl solution. The main component of the TM and TS steels was the ferrite (PDF-06-0696) structure, as shown in Figure 9a and b. After wear testing in the 3.5 wt% NaCl solution, the diffraction peaks for (110), (200), and (211) continued to exist. However, the corrosion product formed on the TM and TS steels after tribocorrosion mainly consisted of Fe_3O_4. The XRD results further identify the iron oxides produced on the sample surfaces, which provide lubricious properties.

Table 6: Content of O and Cl elements in the corrosion scale after 2 h tribocorrosion test (wt%)

Element	Scratch zone		Near-scratch zone		Distant zone	
	TM	TS	TM	TS	TM	TS
O	4.83 ± 1.31	7.14 ± 1.86	22.14 ± 1.98	25.30 ± 1.06	17.27 ± 0.98	12.50 ± 1.10
Cl	Undetected	Undetected	1.89 ± 0.32	2.35 ± 0.37	Undetected	Undetected

Corrosion has a strong influence on the COF of two steels in pure friction compared with tribocorrosion, as observed in Figure 3. The tribocorrosion tests show a lower COF than pure sliding tests for both microstructures. In the study carried out in this article, a higher corrosion rate was observed for martensitic compared to that for sorbite microstructures, which were already reported by previous researchers [44]. Compared with sorbite, martensite is usually formed by rapid cooling of austenite, as a supersaturated solid solution, which leads to the presence of many interior dislocations and microcracks and might provide sites for corrosion initiation. The corrosion resistance of the TM steel was lower than that of the TS steel during tribocorrosion, as shown in Figure 2d, primarily because of the carbide dispersion and precipitation in microstructure of TS steels [45]. Accordingly, a lower COF for TM steels in tribocorrosion is caused by a limited lubricious effect due to the lower amounts of corrosion products compared to that for TS steels. In addition, TM steel has high strength and hardness during the tribocorrosion test; a dominant wear results in that TM steels have narrower scratches in tribocorrosion environments.

Overall, the heat treatments on the microstructures greatly affect the tribocorrosion performance of low-temperature steels. The mechanism of the tribocorrosion process of low-temperature steels in the 3.5 wt% NaCl solution could be established. The friction on the surface of the steel increases the dislocation density and promotes the deformation at the place of scratch on the corroded surface, and the stress caused by friction load is concentrated in the scratch zone. These phenomena increase the electrochemical activity and reduce the corrosion potential of the steels at the scratch site, giving rise to differences in the electrochemical properties at the site between the scratch and other zones. The site in the scratch zone is the anode, and the other is the cathode during the tribocorrosion test, as shown in Figure 10. Figure 8b shows the corrosion reaction during the tribocorrosion process as equations (4) and (5).

$$\text{Anodic reaction: } Fe \rightarrow Fe^{2+} + 2e, \tag{4}$$

$$\text{Cathodic reaction: } \frac{1}{2}O_2 + H_2O + 2e \rightarrow 2OH^-. \tag{5}$$

The anodic reaction mainly occurs in the scratch zone. Friction increases oxygen diffusion in the 3.5 wt% NaCl solution, and the cathodic reaction occurs on the corroded surface. When the ion products (Fe^{2+} and OH^-) reach the solubility product of the corrosion product, the

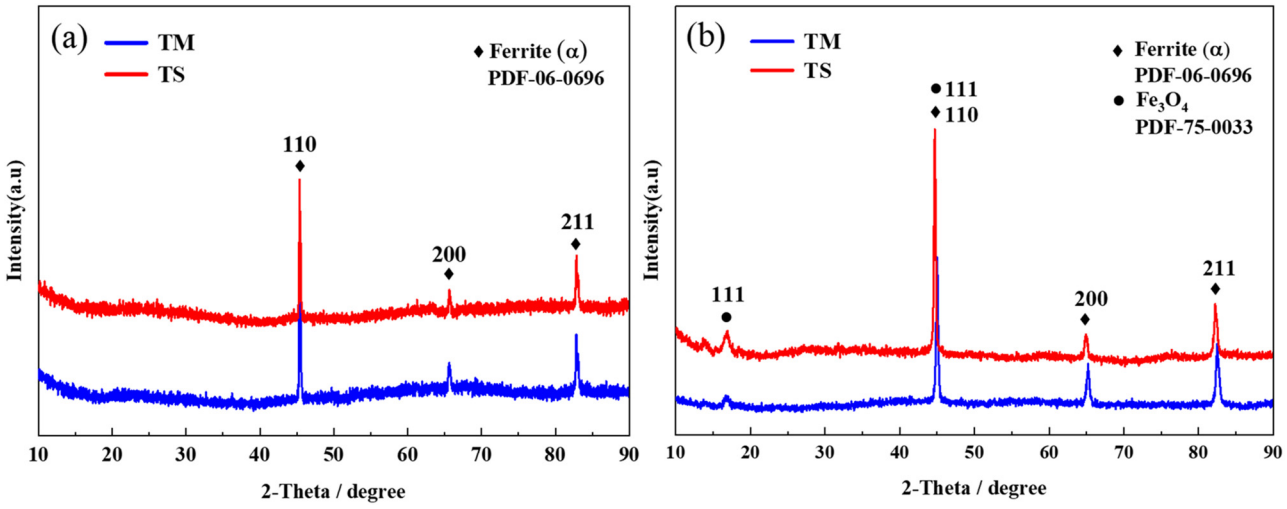

Figure 9: XRD patterns of the surface on the TM and TS steels: (a) before corrosion and (b) after corrosion.

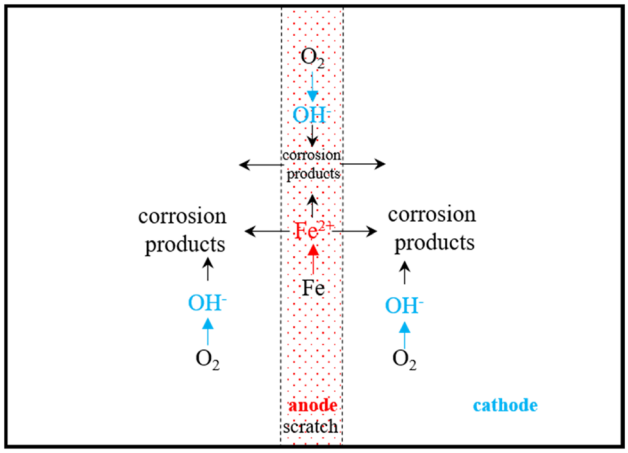

Figure 10: Schematic diagram of the mechanism of the tribocorrosion process for low-temperature steel in 3.5 wt% NaCl solution. Black arrows mean diffusion; red arrows represent anodic reaction; blue arrows indicate a cathodic reaction.

corrosion product forms on the corroded surface [46,47]. The Fe^{2+} formed on the scratch site would diffuse rapidly to the near-scratch site by the stir caused by friction and then combine with OH^- formed and form the corrosion product near the scratch. In addition, the corrosion products formed in the scratch zone diffuse to the near-scratch site by the stir, which explains the abundance of the corrosion products in the near-scratch zone and a few in the scratch zone after the tribocorrosion test.

4 Conclusion

In this study, the microstructures of TM at 250°C and TS structures at 650°C are obtained by heat treatment of FH36 low-temperature steels. Friction, corrosion, and tribocorrosion performance were investigated. The main conclusions are as follows:

1. The outstanding impact toughnessesof the TM steel and TS steel were 239 and 306 J at −60°C, respectively. The tensile strength, yield strength, and hardness of TM steels are better than those of TS steels due to the smaller grain size in the microstructure. The COF of the TM steel was lower than that of the TS steel during the tribocorrosion test.
2. The scratch was deeper and narrower in the TM steel than that in the TS steel during tribocorrosion, and the pitting for the TM steel was more severe than that for the TS steel. The pits were primarily accumulated in the near-scratch zone. Both the corrosion products and Cl^- ions were accumulated near the scratches during tribocorrosion.
3. The corrosion resistance of TM steels was lower than that of the TS steel during tribocorrosion. Compared with pure corrosion, friction can accelerate the adsorption of Cl^- ions and decrease the corrosion potential and corrosion resistance of steel during tribocorrosion.

Acknowledgment: The authors gratefully acknowledge the fund support of Foundation of National Key Research and Development Program (No. 2016YFB0300700), National Natural Science Foundation of China (No. 52071091), and Scientific and Technological Innovation Action Plan of Shanghai (No. 21DZ2205700).

Funding information: This work was financially supported by the Foundation of National Key Research and Development Program (No. 2016YFB0300700), National Natural Science Foundation of China (No. 52071091), and Scientific and Technological Innovation Action Plan of Shanghai (No. 21DZ2205700).

Author contributions: Liang Shi: conceptualization, methodology, writing – original draft, formal analysis, investigation; Da Huo: data curation, software. picture production; Yanhua Lei: validation, supervision, project administration; ShaoPeng Qu: writing – review and editing, methodology, investigation; Xueting Chang: validation, funding acquisition; Yansheng Yin: supervision, funding acquisition.

Conflict of interest: The authors state no conflict of interest.

Data availability statement: The raw/processed data required to reproduce these findings cannot be shared at this time as the data also forms part of an ongoing study.

References

[1] Provencher, J. F., P. J. Thomas, B. M. Braune, B. Pauli, G. Tomy, I. Idowu, et al. Decadal differences in polycyclic aromatic compound (PAC) concentrations in two seabird species in Arctic Canada. *Science of the Total Environment*, Vol. 828, 2022, id. 154088.

[2] Altiparmak, S. O. Arctic drilling in the United States energy revolution context: An accumulated story in environment vs energy contradiction. *Energy Policy*, Vol. 156, No. 1, 2021, id. 112459.

[3] Sun, S. B., Y. F. Zhang, D. S. Wang, X. Wang, Q. J. Zhao, Q. Y. Zhang, et al. Tribocorrosion coupling effect of novel polar marine steel in simulated low temperature seawater. *Tribology*, Vol. 40, No. 5, 2020, pp. 615–625.

[4] Wang, K., L. Wu, Y. Z. Li, and C. Qin. Experimental study on low temperature fatigue performance of polar icebreaking ship steel. *Ocean Engineering*, Vol. 216, No. 3, 2020, id. 107789.
[5] Shen, Y. Y., Y. H. Dong, H. D. Li, X. T. Chang, D. S. Wang, Q. H. Li, et al. The influence of low temperature on the corrosion of EH40 steel in a NaCl solution. *International Journal of Electrochemical Science*, Vol. 13, No. 7, 2018, pp. 6310–6326.
[6] Liu, G. Z., J. M. Wang, J. Q. Zhang, and C. A. Cao. Effect of electrolytic treatment of ballast water on the corrosion behavior of 316L stainless steel. *Acta Metallurgica Sinica*, Vol. 47, No. 12, 2011, pp. 1600–1604.
[7] Bekker, A., K. I. Soal, and K. J. McMahon. Whole-body vibration exposure on board a polar supply and research vessel in open water and in ice. *Cold Regions Science and technology*, Vol. 141, 2017, pp. 188–200.
[8] Yan, S., X. H. Liu, T. S. Liang, J. Q. Chen, and Y. Zhao. Effect of micro-alloying elements on microstructure and mechanical properties in C-Mn-Si quenching and partitioning (Q&P) steels. *Steel Research International*, Vol. 90, No. 1, 2019, id. 1800257.
[9] Shi, Y. C., Z. Q. Li, C. M. Yin, X. L. Yu, and Y. Kou. Effect of alloying elements Cu and Ni on mechanical properties of steel/aluminum laser welded joints. *Optik*, Vol. 255, 2022, id. 168707.
[10] Hafeez, M. A., A. Farooq, B. K. Tayyab, and M. A. Arshad. Effect of thermomechanical cyclic quenching and tempering treatments on microstructure, mechanical and electrochemical properties of AISI 1345 steel. *International Journal of Minerals, Metallurgy and Materials*, Vol. 28, No. 4, 2021, pp. 688–698.
[11] ArslanHafeez, M., M. Usman, M. A. Arshad, and M. AdeelUmer. Nanoindentation-based micro-mechanical and electrochemical properties of quench-hardened, tempered low-carbon steel. *Crystals*, Vol. 10, No. 6, 2020, id. 508.
[12] Aysun, A., D. Kirsever, and A. S. Demirkiran. The Effects of overlapping in electrolytic plasma hardening on wear behavior of carbon steel. *Transactions of the Indian Institute of Metals*, Vol. 75, No. 1, 2022, pp. 27–33.
[13] Li, C. R., X. T. Deng, L. Huang, Y. Jia, and Z. D. Wang. Effect of temperature on microstructure, properties and sliding wear behavior of low alloy wear-resistant martensitic steel. *Wear*, Vol. 442–443, 2020, id. 203125.
[14] Efremenko, V. G., Y. G. Chabak, A. E. Karantzalis, A. Lekatou, I. A. Vakulenko, V. A. Mazur, et al. Plasma Case hardening of wear-resistant high-chromium cast iron. *Strength of Materials*, Vol. 49, No. 3, 2017, pp. 446–452.
[15] Younes, A., P. Nnamchi, J. Medina, P. Perez, V. M. Villapun, F. Badimuro, et al. Wear rate at RT and 100 degrees C and operating temperature range of microalloyed Cu50Zr50 shape memory alloy. *Journal of Alloys and Compounds*, Vol. 817, 2020, id. 153330.
[16] Hafeez, M. A., A. Inam, and A. Farooq. Mechanical and corrosion properties of medium carbon low alloy steel after cyclic quenching and tempering heat-treatments. *Materials Research Express*, Vol. 7, No. 1, 2020, id. 016553.
[17] Katiyar, P. K., S. Misra, and K. Mondal. Comparative corrosion behavior of five microstructures (pearlite, bainite, spheroidized, martensite, and tempered martensite) made from a high carbon steel. *Metallurgical and Materials Transactions A*, Vol. 50A, No. 3, 2019, pp. 1489–1501.
[18] Wei, J., X. X. Fu, J. H. Dong, and W. Ke. Corrosion evolution of reinforcing steel in concrete under dry/wet cyclic conditions contaminated with chloride. *Journal of Materials Science & Technology*, Vol. 28, No. 10, 2012, pp. 905–912.
[19] Liu, Z., E. Y. Liu, S. M. DU, J. H. Zhang, L. P. Wang, H. L. Du, et al. Tribocorrosion behavior of typical austenitic, martensitic, and ferritic stainless steels in 3.5% NaCl solution. *Journal of Materials Engineering and Performance*, Vol. 30, No. 8, 2021, pp. 6284–6296.
[20] Huttunen-Saarivirta, E., L. Kilpi, T. J. Hakala, L. Carpen, and H. Ronkainen. Tribocorrosion study of martensitic and austenitic stainless steels in 0.01 M NaCl solution. *Tribology International*, Vol. 95, 2016, pp. 358–371.
[21] Efremenko, V. G., K. Shimizu, T. Noguchi, A. V. Efremenko, and Y. G. Chabak. Impact-abrasive-corrosion wear of Fe-based alloys: Influence of microstructure and chemical composition upon wear resistance. *Wear*, Vol. 305, No. 1–2, 2013, pp. 155–165.
[22] Ye, Y. W., C. T. Wang, Y. X. Wang, W. Liu, Z. Y. Liu, and X. G. Li. The influence of different metallic counterparts on the tribological performance of nc-CrC/GLC in seawater. *Surface & Coatings Technology*, Vol. 325, 2017, pp. 689–696.
[23] Ma, W. B., H. Y. Luo, Z. Y. Han, L. Y. Zhang, and X. G. Yang. The influence of different microstructure on tensile deformation and acoustic emission behaviors of low-alloy steel. *Materials*, Vol. 13, No. 21, 2020, id. 4981.
[24] Matsumoto, Y., K. Takai, M. Ichiba, T. Suzuki, T. Okamura, and S. Mizoguchi. Reduction of delayed fracture susceptibility of tempered martensitic steel through increased si content and surface softening. *Journal of the Iron & Steel Institute of Japan*, Vol. 99, No. 4, 2013, pp. 236–244.
[25] Zhang, M., X. W. Tong, J. Li, S. Xu, and F. Jia. Microstructure and properties of 25Cr2Ni4MoV steel welded joint under prewelding and post-welding quenching and tempering treatment. *Materials for mechanical engineering*, Vol. 45, No. 1, 2021, pp. 34–40.
[26] Liu, Y., L. X. Du, B. Zhang, H. Y. Wu, and R. D. K. Misra. Significance of finish cooling temperature to microstructure and property relationship of low-carbon V-N-Cr microalloyed high-strength steel. *Journal of Materials Engineering and Performance*, Vol. 28, No. 10, 2019, pp. 6492–6504.
[27] American Bureau of Shipping. *Guide for building and classing vessels intended for navigatioin in polar waters*, US, 2008.
[28] Trausmuth, A., M. R. Ripoll, G. Zehethofer, T. Vogl, and E. Badisch. Impact of corrosion on sliding wear properties of low-alloyed carbon steel. *Wear*, Vol. 328, 2015, pp. 338–347.
[29] De Pellegrin, D. V., A. A. Torrance, and E. Haran. Wear mechanisms and scale effects in two-body abrasion. *Wear*, Vol. 266, No. 1–2, 2009, pp. 13–20.
[30] Trevisiol, C., A. Jourani, and S. Bouvier. Effect of microstructures with the same chemical composition and similar hardness levels on tribological behavior of a low alloy steel. *Tribology International*, Vol. 127, 2018, pp. 389–403.
[31] Wei, M. X., S. Q. Wang, L. Wang, and K. M. Chen. Effect of microstructures on elevated-temperature wear resistance of a hot working die steel. *Journal of Iron and Steel Research (International)*, Vol. 18, No. 10, 2011, pp. 47–53.
[32] Wei, M. X., S. Q. Wang, X. H. Cui, and K. M. Chen. Characteristics of extrusive wear and transition of wear

mechanisms in elevated-temperature wear of a carbon steel. *Tribology Transactions*, Vol. 53, No. 6, 2020, pp. 888–896.
[33] Lopez, A., R. Bayon, F. Pagano, A. Igartua, A. Arredondo, J. L. Arana, et al. Tribocorrosion behaviour of mooring high strength low alloy steels in synthetic seawater. *Wear*, Vol. 338, 2015, pp. 1–10.
[34] Totolin, V., H. Gocerler, M. R. Ripoll, and M. Jech. The role of ferric oxide nanoparticles in improving lubricity and tribo-electrochemical performance during chemical–mechanical polishing. *Tribology Letters*, Vol. 65, No. 1, 2017, id. 20.
[35] Tan, L. W., Z. W. Wang, Y. L. Ma, Y. Yan, and L. J. Qiao. Tribocorrosion investigation of 316L stainless steel: the synergistic effect between chloride ion and sulfate ion. *Materials Research Express*, Vol. 8, No. 8, 2021, id. 086501.
[36] Khobragade, N. N., A. V. Bansod, K. V. Giradkar, A. P. Patil, K. Jagtap, R. Pawde, et al. Effect of concentration and surface roughness on corrosion behavior of Co-Cr-Mo alloy in hyaluronic acid. *Materials Research Express*, Vol. 5, No. 1, 2018, id. 015403.
[37] Liang, D. D., X. S. Wei, T. C. Ma, B. Chen, and J. Shen. Sliding tribocorrosion behavior of Fe-based bulk metallic glass under corrosive environments. *Journal of Non-Crystalline Solids*, Vol. 510, 2019, pp. 62–70.
[38] Natishan, P. M. and W. E. O'Grady. Chloride ion interactions with oxide-covered aluminum leading to pitting corrosion: a review. *Journal of the Electrochemical Society*, Vol. 161, No. 9, 2014, pp. C421–C432.
[39] Wang, X. H., L. Fan, K. K. Ding, L. K. Xu, W. M. Guo, J. Hou, et al. Pitting corrosion of 2Cr13 stainless steel in deep-sea environment. *Journal of Materials Science & Technology*, Vol. 64, 2021, pp. 187–194.
[40] Zhao, Z. H., X. Wang, and M. Wu. Effect of heat treatment on corrosion resistance of 05Cr17Ni4Cu4Nb steel. *Heat Treatment of Metals*, Vol. 43, No. 12, 2018, pp. 109–114.
[41] Lin, Y. C., J. L. Zhang, M. S. Chen, Y. Zhou, and X. Ma. Electrochemical corrosion behaviors of a stress-aged Al-Zn-Mg-Cu alloy. *Journal of Materials Research*, Vol. 31, No. 16, 2016, pp. 2493–2505.
[42] Nazarov, A. and D. Thierry. Application of volta potential mapping to determine metal surface defects. *Electrochimica Acta*, Vol. 52, No. 27, 2007, pp. 7689–7696.
[43] Ren, R. K., S. Zhang, X. L. Pang, and K. W. Gao. A novel observation of the interaction between the macroelastic stress and electrochemical corrosion of low carbon steel in 3.5 wt% NaCl solution. *Electrochimica Acta*, Vol. 85, 2012, pp. 283–294.
[44] Wang, Y. F., Y. T. Zhao, H. H. Ma, and H. P. Ren. Effect of heat treatment on corrosion resistance of 1Cr18Ni9Ti and2Cr13 steel plate welded joint. *Heat Treatment of Metals*, Vol. 46, No. 3, 2021, pp. 7–11.
[45] Yang, H. W., X. Y. Cai, and X. D. Ruan. Effect of preheating and post -weld heat treatment on properties of G20Mn5/P355NL1 dissimilar steel welded joints. *Mechanical Engineer*, Vol. 8, 2019, pp. 170–172.
[46] Farelas, F., M. Galicia, B. Brown, S. Nesic, and H. Castaneda. Evolution of dissolution processes at the interface of carbon steel corroding in a CO_2 environment studied by EIS. *Corrosion Science*, Vol. 52, No. 2, 2010, pp. 509–517.
[47] Sun, J. B., G. A. Zhang, W. Liu, and M. X. Lu. The formation mechanism of corrosion scale and electrochemical characteristic of low alloy steel in carbon dioxide-saturated solution. *Corrosion Science*, Vol. 57, 2012, pp. 131–138.